SPECIAL FEATURE

Vortex filament method as a tool for computational visualization of quantum turbulence

Risto Hänninen[a,1] and Andrew W. Baggaley[b]

[a]O.V. Lounasmaa Laboratory, Aalto University, FI-00076, Aalto, Finland; and [b]School of Mathematics and Statistics, University of Glasgow, Glasgow G12 8QW, United Kingdom

Edited by Katepalli R. Sreenivasan, New York University, New York, NY, and approved December 24, 2013 (received for review August 19, 2013)

The vortex filament model has become a standard and powerful tool to visualize the motion of quantized vortices in helium superfluids. In this article, we present an overview of the method and highlight its impact in aiding our understanding of quantum turbulence, particularly superfluid helium. We present an analysis of the structure and arrangement of quantized vortices. Our results are in agreement with previous studies showing that under certain conditions, vortices form coherent bundles, which allows for classical vortex stretching, giving quantum turbulence a classical nature. We also offer an explanation for the differences between the observed properties of counterflow and pure superflow turbulence in a pipe. Finally, we suggest a mechanism for the generation of coherent structures in the presence of normal fluid shear.

Turbulence in fluid flows is universal, from galactic scales generated by supernova explosions down to an aggressively stirred cup of coffee. There is no debate that turbulence is important, yet no satisfactory theory exists. Turbulence is built by rotational motions, typically over a wide range of scales, interacting and mediating a transfer of energy to scales at which it can be dissipated effectively. The motivation for Küchemann's famous quote "vortices are the sinews and muscles of fluid motions" is clear. If this is true, then quantum turbulence (QT) represents the skeleton of turbulence and offers a method of attacking the turbulence problem in perhaps its simplest form.

QT is a tangle of discrete, thin vortex filaments, each carrying a fixed circulation. It typically is studied in cryogenically cooled helium (1, 2) and, more recently, in atomic Bose–Einstein condensates (3). These substances are examples of so-called quantum fluids: fluids for which certain physical properties cannot be described classically but depend on quantum mechanics. The quantization of vorticity is one marked difference between quantum and classical fluids. Another is their two-fluid nature; they consist of a viscous normal fluid component and an inviscid superfluid component coupled by a mutual friction. The relative densities of these components are temperature dependent.

Despite these marked differences, it is now the consensus opinion that QT is capable of exhibiting many of the statistical properties of classical turbulence, including the famed Kolmogorov scaling (4). Hence, QT has the potential to offer new insights into vortex dynamics and the role they play in the dynamics of turbulence. In addition, QT offers many interesting problems in its own right. However, QT, more so than classical turbulence, suffers from poor visualization of the flow in experiments because of the extremely low temperatures involved. Hence, numerical methods are necessary to aid our understanding of the structure of quantized vortices in different forms of turbulence, acting as a guide for both experiments and theory. In this article, we discuss a widely used numerical model of QT, the vortex filament model (VFM).

VFM

In the VFM, vortices in the superfluid component are considered line defects in which the phase changes by 2π when going around the core. In helium superfluids, the coherence length typically is much smaller than any other characteristic length scale. Therefore, the VFM is a very suitable and convenient scheme to visualize the vortex dynamics in helium superfluids. Within the VFM, the fluid velocity $\mathbf{v}_s$ of the superfluid component is determined simply by the configuration of these quantized vortices and given by the Biot–Savart law (5):

$$\mathbf{v}_s(\mathbf{r},t)=\frac{\kappa}{4\pi}\int\frac{(\mathbf{s}_1-\mathbf{r})\times d\mathbf{s}_1}{|\mathbf{s}_1-\mathbf{r}|^3}. \quad [1]$$

Here, the line integration is along all the vortices and $\kappa=h/m$ is the circulation quantum. For ^{4}He, $m=m_4$ is the bare mass of a helium atom (boson). In the case of ^{3}He, the condensation is made by Cooper pairs, and therefore $m=2m_3$. The Biot–Savart law expresses the Euler dynamics in integral form by assuming a fluid of constant density (6).

Because the vortices are considered to be thin, the small mass of the vortex core may be neglected; therefore, at zero temperature, vortices move according to the local superfluid velocity. Numerically, the Biot–Savart integral is realized easily by having a sequence of points that describe the vortex. The singularity when trying to evaluate the integral at some vortex point, $\mathbf{s}$, may be solved by taking into account that the vortex core size, denoted by a, is finite (5):

$$\mathbf{v}_s=\frac{\kappa}{4\pi}\hat{\mathbf{s}}'\times\mathbf{s}''\ln\left(\frac{2\sqrt{l_+l_-}}{e^{1/2}a}\right)+\frac{\kappa}{4\pi}\int'\frac{(\mathbf{s}_1-\mathbf{s})\times d\mathbf{s}_1}{|\mathbf{s}_1-\mathbf{s}|^3}. \quad [2]$$

Here, $l_\pm$ are the lengths of the line segments connected to $\mathbf{s}$ after discretization, and the remaining integral is over the other segments, not connected to $\mathbf{s}$. Terms $\hat{\mathbf{s}}'$ and $\mathbf{s}''$, where the derivation is with respect to arc length, are (unit) tangent and normal at $\mathbf{s}$, respectively. The first (logarithmic) term on the right-hand side is the so-called local term, which typically gives the major contribution to $\mathbf{v}_s$. In the localized induction approximation (LIA), only this term is preserved (possibly adjusting the logarithmic factor). This is numerically convenient because the work needed per one time step will be proportional to N, which is the number of points used to describe the vortex tangle. Including the nonlocal term also will require $\mathcal{O}(N^2)$ operations. However, LIA is integrable, so in most cases, the inclusion of the nonlocal term is essential to break integrability. For example, under rotation, the correct vortex array is obtained only when the full Biot–Savart integral is used.

At finite temperatures, the motion of the quantized vortex is affected by mutual friction, which originates from scattering of quasiparticles from the vortex cores. Typically, the vortex motion may be described by using temperature-dependent mutual friction parameters α and α', whose values are well known (7, 8). Then, the velocity of the vortex becomes (5, 9)

Author contributions: R.H. and A.W.B. performed research and wrote the paper.

The authors declare no conflict of interest.

This article is a PNAS Direct Submission.

[1]To whom correspondence should be addressed. E-mail: risto.hanninen@aalto.fi.

$$\mathbf{v}_L = \mathbf{v}_s + \alpha\hat{\mathbf{s}}' \times (\mathbf{v}_n - \mathbf{v}_s) - \alpha'\hat{\mathbf{s}}' \times \left[\hat{\mathbf{s}}' \times (\mathbf{v}_n - \mathbf{v}_s)\right]. \quad [3]$$

This equation was derived by Hall and Vinen in the 1950s and was used by Schwarz a few decades later, when the first large-scale computer simulations were conducted. This equation results when one balances the Magnus and drag forces acting on the filament. In general, the normal fluid velocity, $\mathbf{v}_n$, should be solved self-consistently such that vortex motion is allowed to affect the normal component. This methodology may be applied as in refs. 10 and 11; however, most studies in the literature have considered an imposed normal fluid velocity, ignoring any influence of the superfluid component on the normal component, which is more achievable numerically. Indeed, this is a reasonable approximation in ^{3}He, in which the normal component has a viscosity similar to that of olive oil and its motion is laminar. However, it is not appropriate in ^{4}He, in which the normal component is extremely inviscid. Unfortunately, computational limits mean studies with full coupling have had limited scope up to now. For example, in ref. 11, the simulation was limited to an expanding cloud of turbulence and no steady state was reached. What is clear is that the next breed of numerical simulations should seek to follow this work and to try to understand the dynamics of the fully coupled problem.

The presence of solid walls will alter the vortex motion, because the flow cannot go through the walls. For the viscous normal component, one typically uses the no-slip boundary condition, but for an ideal superfluid, the boundary condition is changed to no-flow through the boundary, which implies that the vortex must meet the smooth wall perpendicularly. For plane boundaries, the boundary condition may be satisfied by using image vortices, but with more general boundaries, one has to solve the Laplace equation for the boundary velocity field potential (5). This boundary velocity, plus any additional externally induced velocities, generally must be included in $\mathbf{v}_s$ and $\mathbf{v}_n$ when determining the vortex motion using Eq. **3**. If we are interested purely in homogeneous isotropic turbulence or flow far from the boundaries, then it is typical to work with periodic boundary conditions. These boundaries also may be approximated in the VFM by periodic wrapping; we duplicate the system on surrounding the computational domain with copies of itself: 26 in the case of a periodic cube, for example. The contribution of these duplicate filaments then is included in the Biot–Savart integral (Eq. **3**).

Reconnections. Vortex reconnections are essential in QT, allowing the system to be driven to a nonequilibrium steady state (12). They also change the topology of the tangle (13) and act to transfer energy from 3D hydrodynamic motion to 1D wave motion along the vortices (14). This phenomenon is important if we are to understand the decay of QT in the limit of zero temperature, which we discuss briefly toward the end of the article. Moreover, quantum vortex reconnections not only are important phenomena in quantum fluids, but also are relevant to our general understanding of fluid phenomena.

The VFM cannot handle vortex reconnections directly, because reconnections are forbidden by Euler dynamics. Therefore, an additional algorithm must be used, which changes the topology of two vortices when they become close to each other, essentially a numerical "cut and paste." Several methods have been introduced to model a reconnection (12, 15–17). Importantly, a recent analysis (17) showed that all these algorithms produce very similar results, at least in the case of counterflow turbulence. Microscopically, a single reconnection event was investigated by using the Gross–Pitaevskii model, which is applicable to Bose–Einstein condensates (18, 19). A recent numerical simulation of this microscopic model showed that the minimum separation between neighboring vortices is time asymmetric, as in classical fluids (20). The VFM, on the other hand, results in a more time-symmetric reconnection, in which the distance goes mainly as $d \propto \sqrt{\kappa|t - t_{rec}|}$, where t_{rec} is the reconnection time (19, 21, 22). The prefactor, however, generally is somewhat larger after the reconnection event. This difference results from the characteristic curvatures, which are larger after a typical reconnection event (22, 23).

Interestingly, the results from the VFM are more compatible with experimental results (24) with regard to the scaling of vortex reconnections. Although reconnections must be introduced "by hand" in the VFM, the model seems to capture the essential physics, at least at scales that currently can be probed experimentally.

Tree-Code. A potential drawback of the VFM is the computational time required to perform a simulation that captures the slowly evolving dynamics associated with the largest-scale motions. Although the LIA is computationally advantageous, several studies showed it to be unsuitable for studying fully developed QT (25). However, as we already alluded to, the inclusion of the nonlocal term in Eq. **2** means the scaling of the velocity computation is $\mathcal{O}(N^2)$. A similar problem arose in the field of computational astrophysics, in which calculations to compute the acceleration due to gravity also required $\mathcal{O}(N^2)$ operations. However, since the pioneering work of Barnes and Hut (26), modern astrophysical and cosmological N-body simulations have made use of tree algorithms to enhance the efficiency of the simulation with a relatively small loss of accuracy (27). The major advantage of these methods is the $\mathcal{O}(N\log(N))$ scaling that can be achieved. The essence of the method is to retain nonlocal effects but to take advantage of the r^{-2} scaling in Eq. **2**. Hence, the effect of distant vortices is reasonably small, and an average contribution may be used if it is computed in a systematic way. Several recent studies using the VFM made use of similar tree algorithms (23, 28, 29) to achieve parameter regimes closer to those of actual experiments. It seems clear that tree methods, as in computational astrophysics, will become a standard addition to the VFM.

Limitations. The strongest limitation of the filament model is that it is based on the assumption that all the length scales considered are much larger than the vortex core; therefore, the reconnections typically are made using the above cut-and-paste method. Numerical methods exist that model the vortex core structure and allow better handling of the reconnection process (30). However, if the calculations are extended to core scales, then all the slow large-scale phenomena associated, e.g., with vortex bundles, become numerically unreachable (even with a tree-code) because the time step (required for stability) typically scales as the square of the space resolution. Eulerian dynamics also prevent the generation of sound waves, which are allowed if the vortex dynamics in ^{4}He are modeled by the Gross–Pitaevskii equation. Estimations by Vinen and Niemela (4), however, state that dissipation caused by phonon emission due to reconnections cannot fully explain the large dissipation observed in experiments at low temperatures. This estimation does not take into account the Kelvin wave (KW) cascade (see below), which is predicted to increase the sound emission. To conclude the above, the filament model still requires a physically justified method to model the dissipation at low temperatures, at which the effect of mutual friction vanishes.

Counterflow Turbulence

The earliest experimental studies of QT were reported in a series of groundbreaking papers by Vinen in the 1950s (31–34). In these experiments, turbulence was generated by applying a thermal counterflow, in which the normal and superfluid components flow in opposite directions. This is easily created by applying a thermal gradient, e.g., by heating the fluid at one end. The most common diagnostic to measure is the vortex line density, $L = \Lambda/V$, where Λ is the total length of the quantized vortices and V is the volume of the system; from this, one can compute the typical separation between vortices, the inter vortex spacing $\ell = 1/\sqrt{L}$. This can readily be measured experimentally

using second sound (1), and higher harmonics can probe the structure of the tangle. Numerical simulations have played a crucial role in visualizing the structure of counterflow turbulence and probing the nature of this unique form of turbulence; indeed, it has no classical analog. Some of the very earliest studies using the VFM were performed by Schwarz (12); however, computational limitations forced him to perform an unphysical vortex mixing procedure. A more recent study by Adachi et al. (25) made use of modern computational power and studied the dependence of the steady-state vortex line density on the heat flux of the counterflow. Within the parameter range of the study, there was good agreement with experimental results, vindicating the use of the VFM for counterflow turbulence.

A particularly striking example in which the power to visualize QT helped answer an apparent puzzle is the anomalous decay of counterflow turbulence. Experimentally, it was observed that after switching off the heater, the density of quantized vortices decreased in time, as was expected. In the early stages of the decay, the process was very slow, and it even was observed that the vortex line density might increase, after the drive was turned off. An explanation was provided in ref. 35, in which the authors showed, using the VFM, that the tangle created by counterflow is strongly polarized. However, after they switched off the drive, the vortex lines depolarized. As experimental measurements are based on second sound, this depolarization creates an apparent increase in the measured vortex line density, which is purely an artifact of the measurement process, a truly beautiful result.

A more recent study by Baggaley et al. (23) probed the structure of the superfluid vortices in thermal counterflow by convolving the tangle with the Gaussian kernel to identify any structures in the tangle. In contrast to counterflow, QT generated by more conventional methods, such as mechanical stirring, exhibits the famous Kolmogorov scaling, $E(k) \sim k^{-5/3}$ (36). It is expected (37), and has been observed numerically (38), that this $k^{-5/3}$ scaling is associated with vortex bundling, which may mediate energy transfer in the inertial range. The study of Baggaley et al. (23) showed that this is not the case in counterflow, with the tangle being relatively featureless and consisting of random closed loops, leading to a featureless energy spectrum without motion of many scales, which is the hallmark of classical turbulence.

Visualization of the counterflow turbulence and detailed analysis of the nature of the flow the vortices induce also have direct consequences for analytic theories of QT. For example, Nemirovskii et al. (39) considered the energy spectrum of the velocity field induced by a random set of quantized vortex rings. The analytic spectrum they predicted is quantitatively similar to the energy spectrum obtained numerically by Baggaley et al. (23).

There still are several open and important questions related to the problem of counterflow turbulence. In particular, most numerical simulations have considered the flow away from boundaries to justify the use of periodic boundary conditions. However, this approximation ignores a large amount of important and interesting physics. In the remainder of this section, we consider both counterflow and superflow along a pipe, in which the effects of boundaries are included. Experimentally, pure superflow, in which the normal fluid is held static, is possible by using superleaks at the ends of the pipe. Although initially this may seem purely a Galilean transform of the problem of counterflow, results (40) indicate differences between the two states. However, one should note that for normal fluid, one should have a no-slip boundary condition at the boundaries. Therefore, even with a laminar (parabolic) normal component, the counterflow profile is not fully flat (unlike pure superflow) when both components are involved in generating the counterflow. Using the VFM, we observe that for thermal counterflow, in which the velocity of the normal component is nonzero, a larger average counterflow is needed to achieve a similar vortex line density than when using pure superflow. It is possible that a smaller value of the velocity difference between the two components $(\mathbf{v}_n - \mathbf{v}_s)$, near the boundaries, may explain this result. Turbulence is caused by vortex instability at the boundaries (41), so the level of turbulence that can be supported depends on the counterflow velocity at the boundaries. These results are illustrated in Fig. 1, in which the simulations of counterflow and pure superflow in a pipe with a fixed average flow rate are presented. Future work, following ref. 42, still should be undertaken to further investigate the role of normal fluid turbulence on the observed vortex configuration and vortex line density (43).

Two-Fluid Turbulence

Whereas thermal counterflow is a unique form of turbulence, possible only in quantum fluids, one of the main motivations behind the study of QT is in the so-called semiclassical regime, in which the statistical properties of the turbulence show tantalizing similarities to normal viscous fluids. In particular, this regime has been the focus of several experimental studies (36, 44) in which the classical Kolmogorov energy spectrum and higher-order statistical measures, such as structure functions, show agreement with classical studies. This result also was reproduced by Araki et al. (45), who used the VFM at 0 K to study the evolution of quantized vortices arranged as the classical Taylor–Green vortex.

In addition, the VFM has played an important role in allowing us to visualize the structure of the quantized vortices under the influence of a turbulent normal fluid. Morris et al. (46) performed a particularly influential study in which they coupled a full numerical simulation of the Navier–Stokes equation to the VFM. They observed a locking between vortices in the superfluid component and intense vortical regions in the normal component. This finding built upon an earlier study by Kivotides (47) in which a similar result was obtained, but for a frozen normal fluid velocity field, generated by a turbulent tangle of classical vortex filaments.

In a more recent paper, Kivotides (28) considered the effect of coherent superfluid vortex bundles on an initially stationary normal fluid. Computations were performed using the VFM coupled to the Navier–Stokes equation, with mutual friction accounted for as a forcing term in the Navier–Stokes equation. The author showed that the induced normal-fluid vorticity acquired a morphology similar to that of the structures in the superfluid fraction, and argued that the dynamics of fully developed, two-fluid turbulence depended on interactions of coherent vortical structures in the two components.

Indeed, in classical turbulence, these nonlinear structures, or vortical "worms," appear to play a crucial role in the dynamics of the inertial range (48). In a more recent study, Baggaley et al. (38) developed a procedure to decompose the vortex tangle into a coherent "bundled" component and a random component. Algorithmically, this was achieved by convolving the vortex tangle with a cubic spline:

$$\boldsymbol{\omega}(\mathbf{s}_i) = \kappa \sum_{j=1}^{N} \mathbf{s}_j' W(r_{ij}, h) ds_j, \qquad [4]$$

where $r_{ij} = |\mathbf{s}_i - \mathbf{s}_j|$, $ds_j = |\mathbf{s}_{j+1} - \mathbf{s}_j|$, $W(r,h) = g(r/h)/(\pi h^3)$, h is a characteristic length scale, and

$$g(q) = \begin{cases} 1 - \frac{3}{2}q^2 + \frac{3}{4}q^3, & 0 \le q < 1; \\ \frac{1}{4}(2-q)^3, & 1 \le q < 2; \\ 0, & q \ge 2. \end{cases} \qquad [5]$$

It is appropriate to take h equal to the intervortex spacing, effectively smearing the quantized vorticity to create a continuous vector field in space. Thus, at any point, an effective "vorticity" may be defined; in particular, vortex points with a high vorticity (above a threshold level based on the root-mean-square vorticity) were categorized as part of the coherent component. Analysis of these two components showed that it is the vortex bundles that create the inertial range of the turbulence and that the random component simply is advected in the manner of a passive tracer.

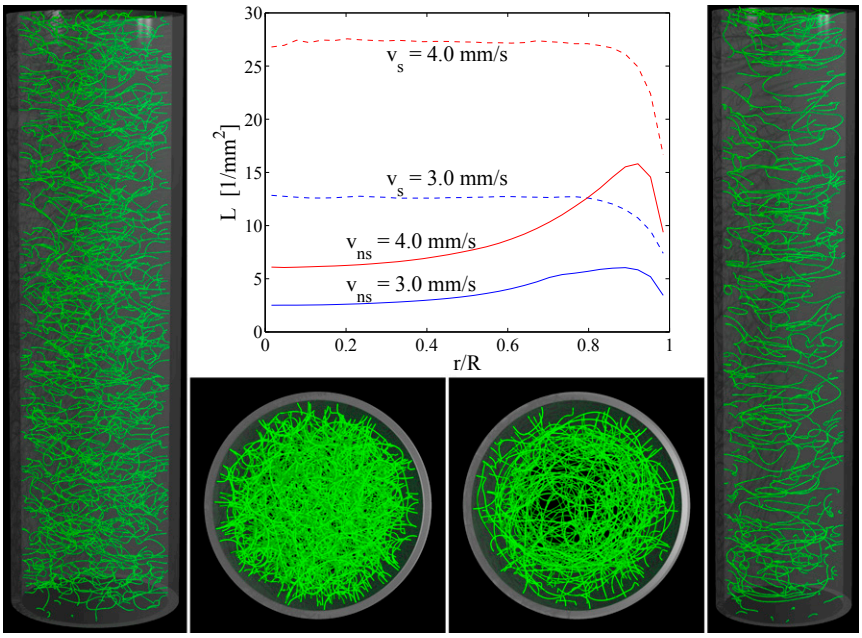

Fig. 1. Counterflow in a cylindrical pipe of radius $R = 1$ mm at $T = 1.9$ K. For vortex structures on the left, the counterflow is caused by pure superflow $v_s = 4.00$ mm/s, and on the right, both components are involved in generating the same counterflow ($v_s = 1.68$ mm/s and $v_n = -2.32$ mm/s) such that the total mass flow is zero. For the normal component, a parabolic velocity profile is used. The middle part of the figure illustrates the vortex line density profile inside the pipe for counterflows of 3.00 mm/s and 4.00 mm/s, using both pure superflow (dashed lines) and thermal counterflow (solid lines), when averaged over a wide time window in the steady state.

In the next section, we consider quantum fluids under rotation, in which we apply this smoothing algorithm to identify previously unidentified transient coherent structures that appear in the system.

Coherent Structures Under Rotation

Rotating fluids are ubiquitous in the universe, so the study of classical fluids under rotation forms a vast topic in its own right. Within the field of viscous fluids, several different flow profiles have been observed, depending on external conditions etc. In helium superfluids, rotation has been used actively to investigate vortex dynamics. The steady state under constant rotation typically is a vortex array that mimics the normal fluid profile. However, before this steady state is reached, turbulence may appear, especially at low temperatures when the mutual friction is low (49–51). The onset and initialization of turbulence have been attributed to the instability that originates from the interaction of the vortex with the container walls (41, 51, 52).

Vortex Front. Recently, perhaps the most investigated coherent structure that appears under rotation has been a propagating turbulent vortex front, which separates a vortex-free region from a twisted vortex cluster behind the front (53–55). The front may be observed in superfluid ^{3}He-B, because the critical velocity for vortex nucleation due to surface roughness can be adjusted to be large enough so that a vortex-free rotation (the so-called Landau state) can be sustained even at relatively large rotation velocities. Now, if vorticity is introduced—for example, by using the Kelvin–Helmholz instability of the A-B phase boundary (56)—a front is generated easily. The propagation velocity of the front is proportional to the dissipation. At the lowest observable temperatures ($T \sim 0.15T_c$), the coupling with the normal fluid almost vanishes, but the energy dissipation still is observed to be finite, orders of magnitude larger than one would obtain from the laminar prediction (54). However, the dissipation of angular momentum remains weak, which is seen from the rotation velocity of the vortex array behind the front. At the lowest temperatures, this rotation velocity drops much below the rotation velocity of the cylindrical cell (55). In a way, the vortex motion decouples from the external reference frame of the rotating cylinder. All these features also are observed in vortex filament simulations (54, 55). Most recently, the VFM helped to develop a simple model that explains the observed behavior (57).

Vortex Bundles During Spin-Up. The structure of the vortex front is a rather natural outcome, because the equilibrium state is a vortex array that tries to mimic the solid-body rotation of the normal component. Here we identify a coherent vortex structure by applying cubic spline smoothing, Eq. **4**, on the vortex structures that appear during the spin-up (by suddenly increasing the rotation velocity) of the superfluid component. Our geometry is a cylinder that is strongly tilted with respect to the rotation axis (58). Initially, we have only a single vortex present, which expands because of the applied flow that is the result of rotation and is nonzero even at zero temperature because of the tilt of the cylinder. As time passes, a polarized vortex tangle develops, which eventually approximates solid-body rotation. Fig. 2 illustrates what happens slightly before the configuration reaches the steady state. Two localized vortex structures (vortex bundles) appear on the opposite sides of the cylinder. In simulations, they are observed at low temperatures with small mutual friction and they appear during the "overshoot" period and quickly merge to the background vorticity. It also is interesting to note that the steady state that approximately mimics the solid-body rotation is reached even at zero temperature, at which the mutual friction coefficients are set to zero. Naturally, there is some small numerical dissipation. A somewhat more peculiar feature of these simulations is that the steady state is not fully static, even at somewhat higher temperatures. This state might appear because the boundary-induced velocity in these simulations is solved only approximately (by using image vortices) (58). Alternatively, the simulations perhaps are stuck in some other local energy minimum, which is not the true minimum. However, these two vortex bundles are just one more example of how superfluid can mimic classical fluids at length scales larger than the intervortex distance by forming coherent structures, even at very low temperatures at which the normal component is vanishingly small.

Spin-Down. The decay of quantized vortices at low temperatures after a sudden stop of rotation (spin-down) has been analyzed in several experiments, in both ^{3}He-B and ^{4}He-II superfluids. The ^{3}He-B experiments, conducted in a cylindrical container, show a laminar-type decay in which the vorticity typically decays as $1/t$ (51, 59). In contrast, the experiments with ^{4}He-II, using a cubical container, show a turbulent decay in which vorticity decreases faster, proportional to $t^{-3/2}$, and is preceded by a strong overshoot just after the rotation stops (50, 60). Although the stronger pinning in ^{4}He-II may favor turbulence over laminar behavior,

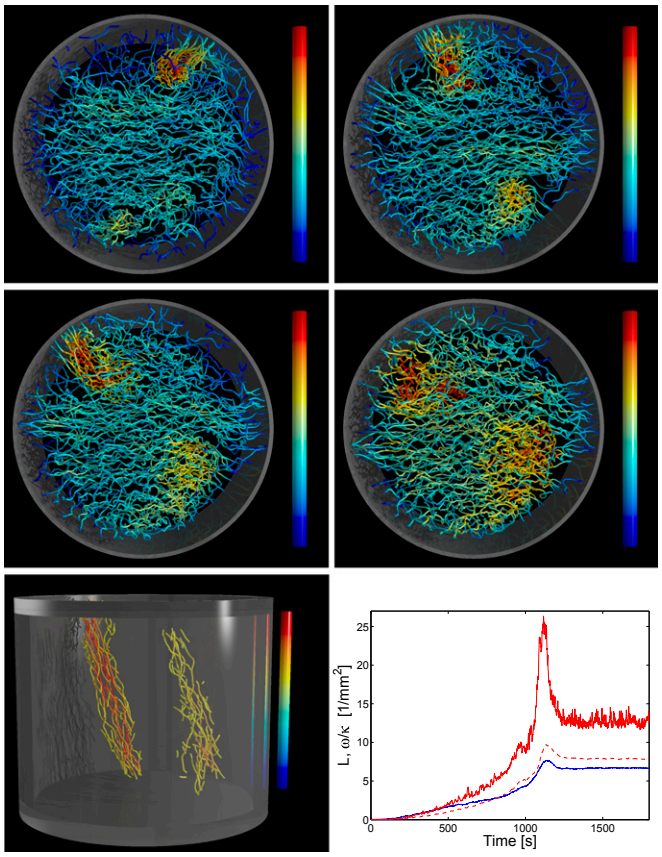

Fig. 2. Coherent structures appearing in a tilted cylinder during the spin-up of the superfluid component. Superfluid ^{3}He-B at $T = 0$ with $R = 3$ mm, $L = 5$ mm, $\Omega = 0.25$ rad/s, and a tilt angle of 30°. The configurations are shown at times t = 1,100 s (*Top Left*), 1,130 s (*Top Right*), 1,140 s (*Middle Left*), and 1,150 s (*Middle Right*), and the color coding illustrates the relative amplitude of the smoothed vorticity. (*Bottom Left*) The coherent structures at t = 1,140 s, where only the coherent part with $\omega > 1.4\omega_{\rm rms}$ is plotted. (*Bottom Right*) The temporal evolution of the vortex line density, L (solid blue line), together with the rms (dashed red line) and maximum vorticity (solid red line).

the recent simulation that used smooth walls, in which pinning was neglected, showed that geometry has a strong effect on decay behavior at low temperatures. Simulations conducted in a sphere, or in a cylinder in which the cylinder axis is close to the initial rotation axis, show a laminar decay in which the vortices remain highly polarized. In contrast, calculations performed in a cubical geometry, or in cases in which the tilt angle for the cylinder is large, indicate turbulent decay (51, 59).

In cylindrically symmetric containers, the decay of vorticity is observed to occur in a laminar fashion, which may be explained by using the Euler equation for inviscid and incompressible flow in uniform rotation. If the initial vorticity corresponds to an equilibrium state given by the initial rotation, Ω_0, and if the rotation is set to rest, then the solution for the radial part of the 2D motion of the vorticity $\Omega_s(t)$ is given by $\Omega_s = \Omega_0/(1 + t/\tau)$ (51, 61). The decay time is given simply by the mutual friction as $\tau = 1/(2\alpha\Omega_0)$. This appropriately models the vorticity in the bulk, in which the polarization is near 100% and the coarse-grained vorticity is spatially homogeneous. In simulations, the dissipation of vorticity (vortex line length) occurs within a thin boundary layer whose thickness increases as temperature (mutual friction dissipation) decreases (51). What happens in the zero temperature limit remains a somewhat open question. Presumably, the thickness of the boundary layer increases as $T \to 0$ so that the laminar decay becomes impossible with vanishing mutual friction.

In cubical containers, or if the cylindrical symmetry is broken, e.g., by strongly tilting the cylinder, the decay shows turbulent behavior, even if the polarization remains nonzero (reflecting the long-surviving vortex array). After an initial overshoot, the decay is faster than in the laminar case. Reconnections here are distributed more evenly in the bulk, indicating turbulence in the whole volume. In addition to the vortex array, the most visible indication of coherent structures is the helical type distortions of this array. This phenomenon is illustrated in Fig. 3, in which we have applied the above vortex-smoothing process, Eq. **4**, on recent spin-down simulations conducted in a cube. These coherent oscillations of the vortex array appear shortly after the rotation is stopped and might be related to the lowest inertial wave resonances. Because the smoothed vorticity resulting from the vortex array is rather uniform and the fluctuations from this level are quite small, the numerical identification of additional structures, if they exist, becomes difficult. However, the faster decay and the apparent absence of different-size coherent structures, typical for Kolmogorov turbulence, might indicate that the decay of type $t^{-3/2}$ is more general than expected.

Decay of a Random Tangle

Of course, the study of turbulent decay is not limited to rotating cases; indeed, the decay of homogeneous isotropic turbulence is

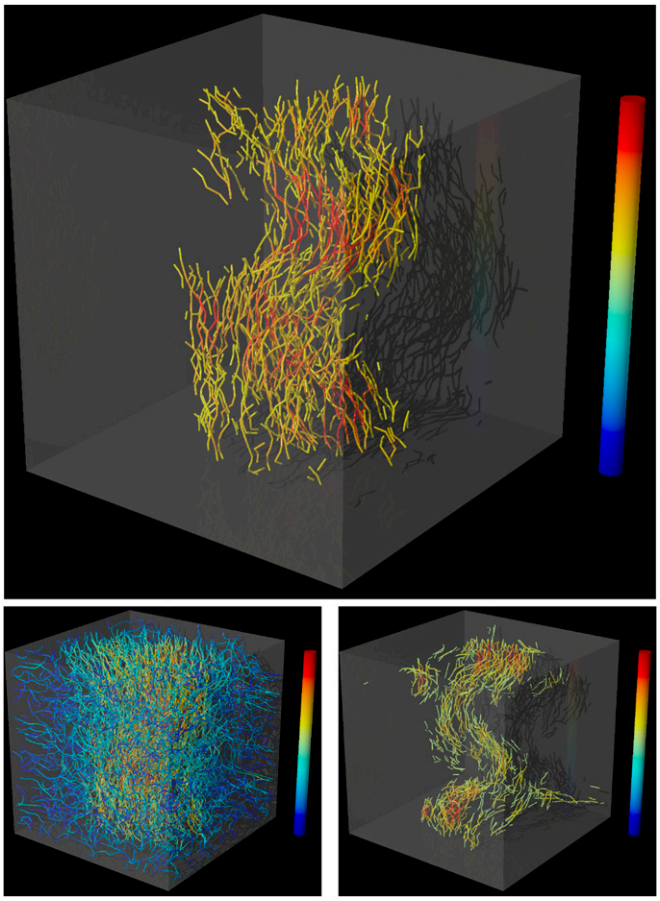

Fig. 3. Decay of vorticity in superfluid ^{3}He-B after a sudden stop of rotation from $\Omega_0 = 0.5$ rad/s. The initial state inside the cube (side 6 mm) was a steady-state vortex array, with a small tilt to break the symmetry. (*Upper*) The coherent vortex part $(\omega > 1.4\omega_{\rm rms})$ at $T = 0.20T_c$ with $t = 87$ s. (*Lower Left*) The full vortex configuration with $\omega_{\rm rms} = 9.23\ {\rm s}^{-1}$ and $\omega_{\rm max} = 21.05\ {\rm s}^{-1}$. (*Lower Right*) The coherent part but at a slightly higher temperature, $T = 0.22T_c$, and t = 64 s. Here, $\omega_{\rm rms} = 10.90\ {\rm s}^{-1}$ and $\omega_{\rm max} = 29.23\ {\rm s}^{-1}$. Coloring of the lines shows the smoothed vorticity, normalized by the maximum smoothed vorticity.

an important field of research. Here, we focus on the decay of QT in the limit of zero temperature. Toward the end of the article, we focus on the physical mechanisms of energy dissipation; here we limit ourselves to the scaling of the decay, as this also is readily measured experimentally. Experiments in helium have revealed two distinct regimes of decay of a random tangle of quantized vortices by monitoring the vortex line density L in time. These are the so-called ultraquantum decay, characterized by $L \sim t^{-1}$, and semiclassical, $L \sim t^{-3/2}$, regimes. Perhaps the most striking example of these two regimes came from a study by Walmsley and Golov (62). By injecting negative ions into superfluid ^{4}He, in the zero temperature limit, they observed the two regimes of turbulence decay. The negative ions (electron bubbles) generated vortex rings, which subsequently interacted, forming a turbulent vortex tangle. After switching off the ion injection, the turbulence then would decay. If the injection time was short, the ultraquantum regime was observed, whereas for a longer injection time, semiclassical behavior was apparent.

Walmsley and Golov argued that the second regime is associated with the classical Kolmogorov spectrum at low wave numbers, whereas the ultraquantum regime is a result of the decay of an unstructured tangle with no dominant large-scale flow. Both regimes also were observed in ^{3}He-B by Bradley et al. (63), who forced turbulence with a vibrating grid.

In a numerical study using the VFM, Fujiyama et al. (64) showed some evidence that a tangle generated by loop injection might exhibit semiclassical behavior and decay such as $L \sim t^{-3/2}$. A more comprehensive study by Baggaley et al. (65) drew inspiration from the experiment of Walmsley and Golov and considered both short and long injection times. This study reproduced both the ultraquantum and the semiclassical regimes and by examining both the curvature of the filaments and the superfluid energy spectrum, confirmed the hypothesis of Walmsley and Golov. In the semiclassical regime, the initial energy distribution was shifted to large scales and a Kolmogorov spectrum was formed. If we now revisit the structure of the tangle in the semiclassical simulation and perform the convolution with a cubic spline, Eq. **5**, then we can see coherent bundling of the vortices, potentially as a result of the strong anisotropy in the loop injection (Fig. 4). In the ultraquantum case, as the injection time is short, the spectrum decays without this energy transfer and very little energy is in the large-scale motions.

Coherent Structures Due to Normal Fluid Shear

Having identified the presence of coherent structures in various systems, it is natural to turn our attention to the generation of coherent structures in QT. Previous studies focused on the role of intense, localized, vortical structures in the normal fluid component (46, 47). The origin of these classical vortex structures often is attributed to the roll-up of vortex sheets by the Kelvin–Helmholtz instability (66). Here, we demonstrate that in QT such a mechanism is viable and that simply the presence of shear in the normal component is enough to lead to the generation of coherent structures. We consider a numerical simulation using the VFM of QT driven by an imposed shear flow in the normal component at $T = 1.9$ K. The normal fluid profile is given by $\mathbf{v}_n = A(\sin(2\pi y/D), 0, 0)$, where $D = 0.1$ cm is the size of the (periodic) domain and $A = 2$ cm/s. The act of the shear in the normal component is to concentrate vortices into areas of low velocity, where they form vortex sheets. In these sheets, vortices lie approximately parallel; therefore, large vortex line densities are created as the dissipative effect of reconnections is small. Once the vortex density in these areas becomes large enough, the sheets visibly buckle and begin the roll-up process, as may be seen in Fig. 5. This effect might be important in several scenarios, particularly in the onset of normal fluid turbulence in counterflow.

Future Challenges

In addition to topics covered here, the VFM also has shown it may be a useful tool in interpreting experiments in which the motion of tracer particles is used to visualize the quantum turbulence, or in investigating the properties of the vortex tangle generated by oscillating structures. In the future, coupled

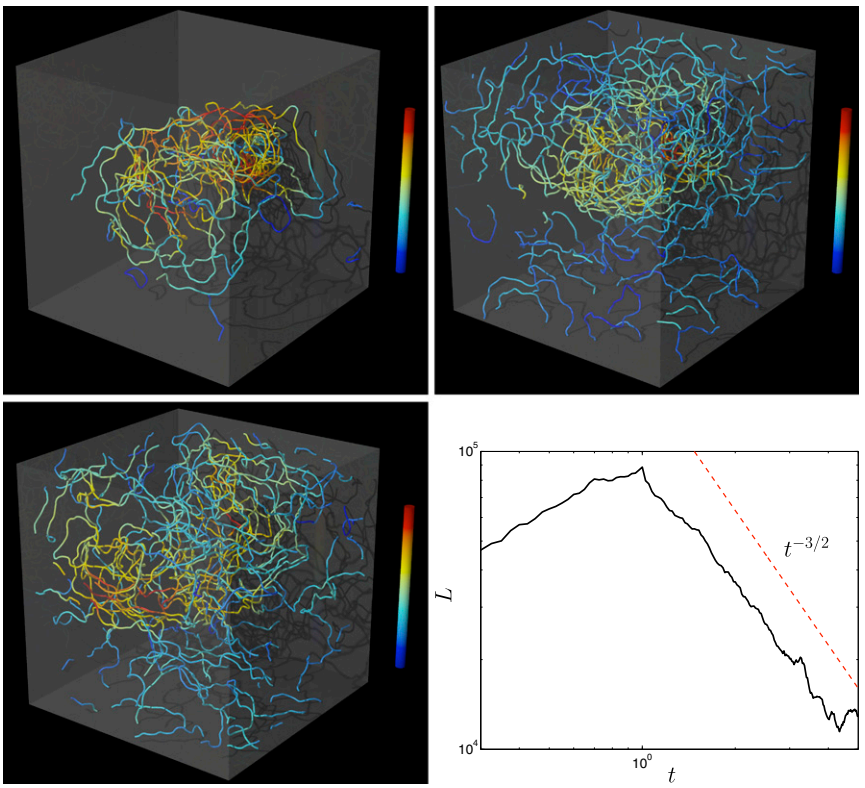

Fig. 4. Decay of semiclassical turbulence in superfluid ^{4}He. The vortex configurations are plotted at $t = 0.1$ s (*Upper Left*), $t = 0.75$ s (*Upper Right*), and $t = 1.1$ s (*Lower Left*). The coloring of the lines shows the smoothed vorticity, normalized by the maximum smoothed vorticity ($\omega_{max} = 16.31$, 37.7, and 29.3 s^{-1}, respectively). The shaded box shows the periodic domain of the simulation, a cube of side 0.03 cm. The corresponding vortex line densities are 4.1×10^4, 7.8×10^4, and 7.5×10^4 cm^{-2}. (*Lower Right*) The evolution of the vortex line density and the semiclassical scaling.

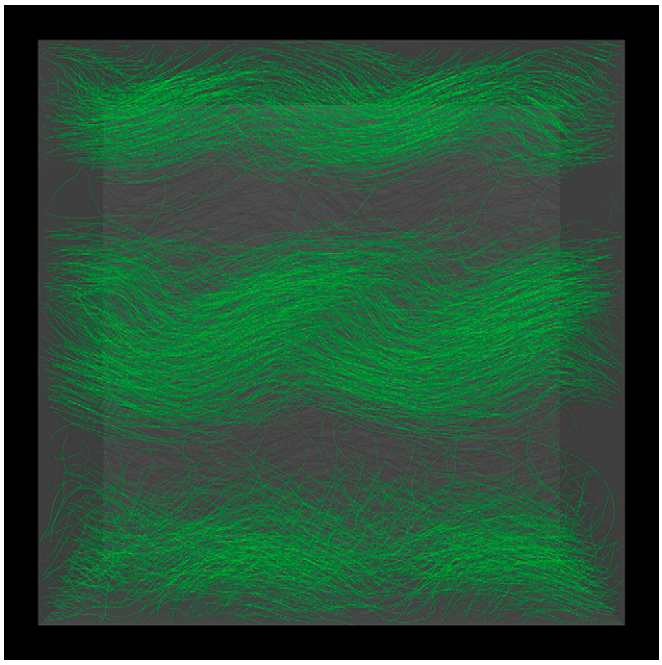

Fig. 5. Sheets of quantized vortices beginning to roll up as a result of the Kelvin–Helmholtz instability. The vortex sheets are created by an imposed shear in the normal component.

dynamics with normal fluid will be essential in understanding the dynamics of the normal component. Currently, the dissipation in the zero temperature limit is perhaps the most interesting topic in the field of QT. In the following sections, we concentrate on two topics strongly related to this, namely the KW cascade and the possible bottleneck appearing at scales on the order of the average intervortex distance.

KW Cascade. At relatively large temperatures (greater than 1 K in ^{4}He), kinetic energy contained in the superfluid component is transferred by mutual friction to the normal fluid and subsequently into heat via viscous heating. A constant supply of energy (continuous stirring, for example) is needed to maintain the turbulence. At very low temperatures, the normal fluid is negligible, but despite the absence of mutual friction, the turbulence still decays (62, 63). The KW cascade (14) perhaps is the most important mechanism proposed to explain this surprising effect.

KWs are a classical phenomenon (67), rotating sinusoidal or helical perturbations of the core of a concentrated vortex filament. The KW cascade is the process in which the nonlinear interaction of KWs creates higher-frequency modes. At very high frequencies (at which the wavelength is atomic scale), sound is efficiently radiated away (phonon emission). Hence, in contrast to classical turbulence, in which the energy sink is viscous, in QT the energy sink is acoustic. Crucially, KWs are generated easily in QT, in which vortex reconnections typically create a high-curvature cusp (68), which acts as a mechanism to transfer energy from 3D hydrodynamic turbulence to 1D wave turbulence along the vortex filaments.

Currently, two regimes are believed to exist in the KW cascade, one corresponding to large-amplitude waves and the other to a low-amplitude, weakly nonlinear regime, in which the theory of wave turbulence can be applied (69). It is in this weakly nonlinear regime where the VFM may play a crucial role in distinguishing several proposed theories (70–72). The key prediction of each theory is in the spectrum of kelvon occupation numbers, each of which gives different power-law scalings, $n_k \sim k^{-\alpha}$. In particular, Kozik and Svistunov (70) proposed $\alpha = 17/5$, but L'vov et al. (71) claimed this spectrum was invalid because of the assumption of locality of interactions and proposed a nonlocal theory that predicted $\alpha = 11/3$. Although it is not simply the spectrum of n_k that distinguishes these two theories, it perhaps is the easiest statistic to compute with the VFM, as n_k is related to the KW amplitudes. However, the fact that these exponents are so similar clearly presents a huge computational challenge if one is to provide strong evidence for either theory. Few attempts have been made to determine the exponent α (73–75), but we would argue that no convincing evidence for either theory has been demonstrated yet. One reason is the difficulty in identifying a KW on a curved vortex (76).

Bottleneck? Although much attention has been focused on the KW cascade, perhaps of more importance, particularly in experimental interpretation, is how the 1D KW cascade matches the 3D hydrodynamic energy spectrum. Once again, rival theories have been proposed by Kozik and Svistunov and by L'vov et al. To summarize the situation briefly, L'vov et al. predict a bottleneck in energy, which is required for continuity in the energy flux at the crossover scale; therefore, one should expect an increase in the vortex line density at scales on the order of the intervortex spacing, ℓ. This is countered by Kozik and Svistunov (77), who argue for several different reconnection regimes between the Kolmogorov and KW spectra that do not create such a bottleneck. However, another view has been provided by Sonin (72), who argues that the bottleneck might be totally absent. Again, this is an open and important question that has yet to be studied in detail using the VFM. The large range of scales involved means that new numerical approaches, such as the tree-code discussed earlier, will be vital for any progress to be made.

Conclusions

To summarize, we hope the reader will agree that the VFM has proven to be a valuable tool in the study of superfluid turbulence and quantized vortex dynamics. Here, we have illustrated that the quantized vortices can form coherent structures, even at low temperatures at which the fraction of normal component is small, and give QT a classical nature. The formation of coherent structures is also shown to readily appear in the presence of normal fluid shear, resulting in the roll-up of vortex sheets due to classical Kelvin–Helmholtz instability. Of course, despite some of the success stories we have described here, there still is much work to be done. Much attention in the literature has focused on the KW cascade, and perhaps rightly so. However, other decay mechanisms, such as loop emission due to vortex reconnections (78), warrant further investigation. Indeed, they may play an important role in the decay of the unstructured "Vinen tangle."

The field itself of course will be driven by experimental studies, and it is an exciting time with many new investigations planned in the near future. Nevertheless, the role of the VFM in helping to analyze and interpret this experimental data and to test, refine, and motivate analytic theories remains important.

In addition, superfluid turbulence is not just found in the laboratory. There are important astrophysical applications. Current theory strongly suggests that the outer core of neutron stars consists of neutrons in a superfluid state. Because of incredibly rapid rotation, we would expect this superfluid to be threaded by quantized vortices pinned to the solid outer crust. Interesting phenomena, such as rapid changes in the rotation rate, are observed and thought to be related to the behavior of the quantized vortices (79). Such a system might reasonably be modeled with the VFM, and it remains an interesting problem awaiting such an investigation.

ACKNOWLEDGMENTS. R.H. thanks N. Hietala for useful discussions and CSC - IT Center for Science Ltd. for the allocation of computational resources. This work is supported by the European Union Seventh Framework Programme (FP7/2007-2013, Grant 228464 Microkelvin). R.H. acknowledges financial support from the Academy of Finland.

1. Donnelly RJ (1991) *Quantized Vortices in Helium II* (Cambridge Univ Press, Cambridge, UK).
2. Barenghi CF, Donnelly RJ, Vinen WF (2001) *Quantized Vortex Dynamics and Superfluid Turbulence*, Lecture Notes in Physics (Springer, Berlin), Vol 571.
3. Henn EAL, Seman JA, Roati G, Magalhães KMF, Bagnato VS (2009) Emergence of turbulence in an oscillating bose-einstein condensate. *Phys Rev Lett* 103(4):045301.
4. Vinen WF, Niemela JJ (2002) Quantum turbulence. *J Low Temp Phys* 128(5-6):167–231.
5. Schwarz KW (1985) Three-dimensional vortex dynamics in superfluid ^{4}He: Line-line and line-boundary interactions. *Phys Rev B Condens Matter* 31(9):5782–5804.
6. Saffman PG (1992) *Vortex Dynamics* (Cambridge Univ Press, Cambridge, UK).
7. Bevan TDC, et al. (1997) Vortex mutual friction in superfluid ^{3}He. *J Low Temp Phys* 109(3-4):423–459.
8. Donnelly RJ, Barenghi CF (1998) The observed properties of liquid helium at saturated vapour. *J Phys Chem Ref Data* 27(6):1217–1274.
9. Hall HE, Vinen WF (1957) The rotation of liquid helium II. The theory of mutual friction in uniformly rotation helium II. *Proc R Soc Lond A Math Phys Sci* 238(1213): 215–234.
10. Kivotides D, Barenghi CF, Samuels DC (2000) Triple vortex ring structure in superfluid helium II. *Science* 290(5492):777–779.
11. Kivotides D (2011) Spreading of superfluid vorticity clouds in normal-fluid turbulence. *J Fluid Mech* 668(2):58–75.
12. Schwarz KW (1988) Three-dimensional vortex dynamics in superfluid ^{4}He: Homogeneous superfluid turbulence. *Phys Rev B Condens Matter* 38(4):2398–2417.
13. Poole DR, Scoffield H, Barenghi CF, Samuels DC (2003) Geometry and topology of superfluid turbulence. *J Low Temp Phys* 132(1-2):97–117.
14. Svistunov BV (1995) Superfluid turbulence in the low-temperature limit. *Phys Rev B Condens Matter* 52(5):3647–3653.
15. Kondaurova L, Nemirovskii SK (2008) Numerical simulations of superfluid turbulence under periodic conditions. *J Low Temp Phys* 150(3-4):415–419.
16. Tsubota M, Araki T, Nemirovskii SK (2000) Dynamics of vortex tangle without mutual friction in superuid ^{4}He. *Phys Rev B* 62(17):11751–11762.
17. Baggaley AW (2012) The sensitivity of the vortex filament method to different reconnection models. *J Low Temp Phys* 168(1-2):18–30.
18. Koplik J, Levine H (1993) Vortex reconnection in superfluid helium. *Phys Rev Lett* 71(9):1375–1378.
19. Zuccher S, Caliari M, Baggaley AW, Barenghi CF (2012) Quantum vortex reconnections. *Phys Fluids* 24(12):125108.
20. Hussain F, Duraisamy K (2011) Mechanics of viscous vortex reconnection. *Phys Fluids* 23(2):021701.
21. de Waele AT, Aarts RG (1994) Route to vortex reconnection. *Phys Rev Lett* 72(4): 482–485.
22. Hänninen R (2013) Dissipation enhancement from a single vortex reconnection in superfluid helium. *Phys Rev B* 88:054511.
23. Baggaley AW, Sherwin LK, Barenghi CF, Sergeev YA (2012) Thermally and mechanically driven quantum turbulence in helium II. *Phys Rev B* 86(10):104501.
24. Paoletti MS, Fisher ME, Lathrop DP (2010) Reconnection dynamics for quantized vortices. *Physica D* 239(14):1367–1377.
25. Adachi H, Fujiyama S, Tsubota M (2010) Steady-state counterflow quantum turbulence: Simulations of the vortex filaments using the full Biot-Savart law. *Phys Rev B* 81(10):104511.
26. Barnes J, Hut P (1986) A hierarchical O(N log N) force-calculation algorithm. *Nature* 324(6096):446–449.
27. Bertschinger E (1998) Simulations of structure formation in the universe. *Annu Rev Astron Astrophys* 36(1):599–654.
28. Kivotides D (2007) Relaxation of superfluid vortex bundles via energy transfer to the normal fluid. *Phys Rev B* 76(5):054503.
29. Baggaley AW, Barenghi CF (2011) Vortex-density fluctuations in quantum turbulence. *Phys Rev B* 84(2):020504.
30. Kivotides D, Leonard A (2003) Computational model of vortex reconnection. *Europhys Lett* 63(3):354–360.
31. Vinen WF (1957) Mutual friction in a heat current in liquid helium II. I. Experiments on steady heat currents. *Proc R Soc Lond A Math Phys Sci* 240(1220):114–127.
32. Vinen WF (1957) Mutual friction in a heat current in liquid helium II. II. Experiments on transient. *Proc R Soc Lond A Math Phys Sci* 240(1220):128–143.
33. Vinen WF (1957) Mutual friction in a heat current in liquid helium II. III. Theory of the mutual friction. *Proc R Soc Lond A Math Phys Sci* 242(1231):493–515.
34. Vinen WF (1958) Mutual friction in a heat current in liquid helium II. IV. Critical heat currents in wide channels. *Proc R Soc Lond A Math Phys Sci* 243(1234):400–413.
35. Barenghi CF, Gordeev AV, Skrbek L (2006) Depolarization of decaying counterflow turbulence in He II. *Phys Rev E Stat Nonlin Soft Matter Phys* 74(2 Pt 2):026309.
36. Maurer J, Tabeling P (1998) Local investigation of superfluid turbulence. *Europhys Lett* 43(1):29–34.
37. L'vov VS, Nazarenko SV, Rudenko O (2007) Bottleneck crossover between classical and quantum superfluid turbulence. *Phys Rev B* 76(2):024520.
38. Baggaley AW, Laurie J, Barenghi CF (2012) Vortex-density fluctuations, energy spectra, and vortical regions in superfluid turbulence. *Phys Rev Lett* 109(20):205304.
39. Nemirovskii SK, Tsubota M, Araki T (2002) Energy spectrum of the random velocity field induced by a Gaussian vortex tangle in He II. *J Low Temp Phys* 126(5-6):1535–1540.
40. Chagovets TV, Skrbek L (2008) Steady and decaying flow of He II in a channel with ends blocked by superleaks. *Phys Rev Lett* 100(21):215302.
41. de Graaf R, et al. (2008) The dynamics of vortex generation in superfluid ^{3}He-B. *J Low Temp Phys* 153(5-6):197–227.
42. Baggaley AW, Laizet S (2013) Vortex line density in counterflowing He II with laminar and turbulent normal fluid velocity profiles. *Phys Fluids* 25(11):115101.
43. Tough JT (1982) *Superfluid Turbulence, Progress in Low Temperature Physics*, ed Brewer DF (North-Holland, Amsterdam), Vol VIII, pp 133–219.
44. Salort J, Chabaud B, Lévêque E, Roche P-E (2012) Energy cascade and the four-fifths law in superfluid turbulence. *Europhys Lett* 97(3):34006.
45. Araki T, Tsubota M, Nemirovskii SK (2002) Energy spectrum of superfluid turbulence with no normal-fluid component. *Phys Rev Lett* 89(14):145301.
46. Morris K, Koplik J, Rouson DW (2008) Vortex locking in direct numerical simulations of quantum turbulence. *Phys Rev Lett* 101(1):015301.
47. Kivotides D (2006) Coherent structure formation in turbulent thermal superfluids. *Phys Rev Lett* 96(17):175301.
48. Farge M, Schneider K, Pellegrino G, Wray AA, Rogallo RS (2003) Coherent vortex extraction in three-dimensional homogeneous turbulence: Comparison between CVS-wavelet and POD-Fourier decompositions. *Phys Fluids* 15(10):2886–2896.
49. Finne AP, et al. (2003) An intrinsic velocity-independent criterion for superfluid turbulence. *Nature* 424(6952):1022–1025.
50. Eltsov VB, et al. (2009) Turbulent dynamics in rotating helium superfluids. *Progress in Low Temperature Physics*, eds Tsubota M, Halperin WP (Elsevier, Amsterdam), Vol XVI, pp 45–146.
51. Eltsov VB, et al. (2010) Vortex formation and annihilation in rotating superfluid ^{3}He-B at low temperatures. *J Low Temp Phys* 161(5-6):474–508.
52. Finne AP, et al. (2006) Vortex multiplication in applied flow: A precursor to superfluid turbulence. *Phys Rev Lett* 96(8):085301.
53. Eltsov VB, et al. (2006) Twisted vortex state. *Phys Rev Lett* 96(21):215302.
54. Eltsov VB, et al. (2007) Quantum turbulence in a propagating superfluid vortex front. *Phys Rev Lett* 99(26):265301.
55. Hosio JJ, et al. (2011) Superfluid vortex front at T→0: Decoupling from the reference frame. *Phys Rev Lett* 107(13):135302.
56. Blaauwgeers R, et al. (2002) Shear flow and Kelvin-Helmholtz instability in superfluids. *Phys Rev Lett* 89(15):155301.
57. Hosio JJ, et al. (2013) Energy and angular momentum balance in wall-bounded quantum turbulence at very low temperatures. *Nat Commun* 4:1614.
58. Hänninen R (2009) Rotating inclined cylinder and the effect of the tilt angle on vortices. *J Low Temp Phys* 156(3-6):145–162.
59. Eltsov VB, et al. (2010) Stability and dissipation of laminar vortex flow in superfluid ^{3}He-B. *Phys Rev Lett* 105(12):125301.
60. Walmsley PM, Golov AI, Hall HE, Levchenko AA, Vinen WF (2007) Dissipation of quantum turbulence in the zero temperature limit. *Phys Rev Lett* 99(26):265302.
61. Sonin EB (1987) Vortex oscillations and hydrodynamics in rotating superfluids. *Rev Mod Phys* 59(1):87–155.
62. Walmsley PM, Golov AI (2008) Quantum and quasiclassical types of superfluid turbulence. *Phys Rev Lett* 100(24):245301.
63. Bradley DI, et al. (2006) Decay of pure quantum turbulence in superfluid ^{3}He-B. *Phys Rev Lett* 96(3):035301.
64. Fujiyama S, et al. (2010) Generation, evolution and decay of pure quantum turbulence: A full Biot-Savart simulation. *Phys Rev B* 81(18):180512.
65. Baggaley AW, Barenghi CF, Sergeev YA (2012) Quasiclassical and ultraquantum decay of superfluid turbulence. *Phys Rev B* 85(6):060501.
66. Vincent A, Meneguzzi M (1994) The dynamics of vorticity tubes in homogeneous turbulence. *J Fluid Mech* 258(1):245–254.
67. Thomson W (1880) Vibrations of a columnar vortex. *Philos Mag* 10(61):155–168.
68. Kivotides D, Vassilicos JC, Samuels DC, Barenghi CF (2001) Kelvin waves cascade in superfluid turbulence. *Phys Rev Lett* 86(14):3080–3083.
69. Nazarenko SV (2011) *Wave Turbulence* (Springer, Heidelberg).
70. Kozik E, Svistunov B (2004) Kelvin-wave cascade and decay of superfluid turbulence. *Phys Rev Lett* 92(3):035301.
71. L'vov VS, Nazarenko S (2010) Spectrum of Kelvin-wave turbulence in superfluids. *JETP Lett* 91(8):428–434.
72. Sonin EB (2012) Symmetry of Kelvin-wave dynamics and the Kelvin-wave cascade in the $T = 0$ superfluid turbulence. *Phys Rev B* 85(10):104516.
73. Vinen WF, Tsubota M, Mitani A (2003) Kelvin-wave cascade on a vortex in superfluid ^{4}He at a very low temperature. *Phys Rev Lett* 91(13):135301.
74. Kozik E, Svistunov B (2005) Scale-separation scheme for simulating superfluid turbulence: Kelvin-wave cascade. *Phys Rev Lett* 94(2):025301.
75. Baggaley AW, Barenghi CF (2011) Spectrum of turbulent Kelvin-waves cascade in superfluid helium. *Phys Rev B* 83(13):134509.
76. Hänninen R, Hietala N (2013) Identification of Kelvin waves: Numerical challenges. *J Low Temp Phys* 171(5-6):485–496.
77. Kozik E, Svistunov B (2008) Kolmogorov and Kelvin-wave cascades of superfluid turbulence at $T = 0$: What lies between. *Phys Rev B* 77(6):060502.
78. Kursa M, Bajer K, Lipniacki T (2011) Cascade of vortex loops initiated by a single reconnection of quantum vortices. *Phys Rev B* 83(1):014515.
79. Andersson N, Glampedakis K, Ho WCG, Espinoza CM (2012) Pulsar glitches: The crust is not enough. *Phys Rev Lett* 109(24):241103.